

**Assessment of Wildland-Urban Interface Fire Risks and Hazards
for City of Edmonton Buildings and Infrastructure:
A Crowdsensing Framework**

Research Team: Asdrubal Cheng Cen, Daniel Jozi, and Mohammed Afghani

Research Lead: Dr. Nima Shirzad-Ghaleroudkhani

Principal Investigator: Prof. Mustafa Gül

Department of Civil and Environmental Engineering

University of Alberta

May 2023

Table of Contents

Abstract	1
1 Introduction	1
2 Satellite Image Analysis	4
2.1 Topographic and Priority Zone Analysis	5
2.2 Fuel Identification and Classification	9
3 Street-level Crowdsensing Video Analysis	17
3.1 Fuel Identification and Classification	17
3.2 Crown Base Height Estimation	19
3.3 Grassland Curing Assessment.....	24
4 Fire Behavior Analysis	29
4.1 Rate of Spread	29
4.2 Head Fire Intensity.....	34
5 Graphical User Interface.....	37
6 Conclusions and Future Work.....	40
7 Funding Acknowledgement.....	41
References.....	42

Abstract

Due to the increasing consequences of climate change, many areas in Alberta are becoming prone to wildfires that threaten urban infrastructure, defined as the Wildland-Urban Interface (WUI) fires. In the last decade, wildfires in Canada have burned an area equivalent to 2.9 million hectares. It is, therefore, necessary to develop a more advanced framework to determine fire behaviour parameters such as rate of spread (ROS) and head fire intensity (HFI) at the micro-scale. This would enable urban decision-makers to take decisive actions toward more resilient infrastructure systems.

The framework proposed in this research employs street-level crowdsensing videos to extract up-to-date micro-scale fuel information for the fire behaviour prediction system. Automated satellite imagery analysis is also applied to extract fuel information in areas with limited crowdsensing data availability. AI-based object detection and image segmentation algorithms have been developed to detect fuel types and features from the image data.

The Kinsmen Sport Centre in Edmonton was studied as the building of interest, and the inputs from crowdsensing data for August 16th and November 1st, 2022 were used to calculate the rate of spread and head fire intensity. This study demonstrates the potential of crowdsensing-based methods to extract detailed and up-to-date fuel information necessary for developing strategies to mitigate fire risks in WUI areas.

1 Introduction

Due to the increasing risk of climate change in the coming years, many areas in Canada where wildlands and urban development meet are becoming more susceptible to wildfires. National Guide for Wildland-Urban Interface (WUI) Fires [1], issued by the National Research Council of

Canada, estimated that 5,553 fires happened in the last decade, damaging around 2.9 million hectares of wildland. Urban areas, particularly those situated close to wildlands, are becoming more vulnerable as they are located within or near densely forested areas. A recent example is the fire that occurred in the city of Lytton, BC on June 30, 2021, which destroyed 151 buildings and claimed the lives of 2 people [2]. According to a summary report to the British Columbia FireSmart Committee, a fundamental cause of the disaster was the lack of appropriate mitigation on vulnerability and exposure of structures to fire-prone wildland areas [2]. In regards to the City of Edmonton, river valley fires in 2016 [3] and a most recent one in 2023 [4] are examples of how important could be the WUI fire risk assessment for the resiliency of urban buildings and infrastructure in a resilient city.

Although several empirical and accurate approaches have been formulated to estimate the fire behaviour in forest fires such as Anderson [5] and Van Wagner [6], they have limited approaches to estimate the risk of a wildland fire near buildings and human-made structures. On the other hand, National Guide for WUI Fires [1] provides recommendations to reduce the WUI fire risk on buildings yet it offers a simplistic approach to estimate the fire behaviour near building areas compared to the empirical approaches, presumably due to the lack of real-time data availability. Effective features such as seasonal changes in deciduous trees, the curing effect on grasses, and the crown base height on conifers, are fundamental parameters that are crucial in estimating fire risk.

Most common wildfire risk assessments are performed using satellite and aerial images. Regarding WUI, employing such technologies for urban vegetation mapping has been the subject of previous studies [7]. These technologies allow researchers to capture high-resolution images from different angles, making it easier to map urban vegetation cover. One of the advantages of using satellite imagery for urban vegetation mapping is its ability to cover large areas quickly and efficiently. Additionally, satellite imagery can provide data over extended periods, allowing researchers to analyze vegetation cover changes over time. UAV imagery provides even higher

resolution images and is useful for mapping small areas or capturing images of vegetation in difficult-to-reach locations. However, the use of satellite and UAV imagery has some disadvantages. Atmospheric conditions such as cloud cover and haze can reduce the quality and accuracy of these images. The cost of obtaining and processing satellite or UAV imagery can also be high, which may limit its use in some research projects. Moreover, it is important to note that these methods may not provide dynamic and up-to-date information about fuel conditions due to the fact that they are not updated frequently. Therefore, while remote sensing techniques can be an effective tool for the initial mapping and monitoring of urban vegetation, they should be integrated with ground-based regularly-updated sources for a more comprehensive understanding of vegetation dynamics in urban areas.

Recent literature has highlighted trends in assessing urban fuels along street networks, which have gained attention and are promoted by a larger number of municipalities [8]. The first trend is the growing availability of low-cost, detailed, and crowd-sourced street-level imagery, which comprises photographs of street scenes taken from the ground [9, 10]. The second trend is the success of Convolutional Neural Networks in extracting abstract features and objects in imagery, out-competing traditional methods [11]. Street-level imagery is being used to estimate the percentage of detected canopy-covered pixels relative to the total number of pixels in an image, which quantifies the “perceived urban canopy cover” [12]. Similarly, Li et al. [13] used green pixels in street view scenes to estimate the percentage of vegetation in streets.

The technique of using street-level imagery along with deep learning has been employed to improve the accuracy of tree inventories based on coarse street addresses with accurate geographic coordinates [14]. Laumer et al. [14] utilized this method and were able to match 38% of over 50,000 identified street trees to their respective street-level addresses. Meanwhile, Wegner et al. [15] developed a workflow that combines the results of Faster Region Convolutional Neural Network (R-CNN) tree detection from Google Street View (GSV) and aerial imagery with data from Google Maps in a probabilistic model to automatically detect and geolocate street trees. They

were able to classify 18 different species among the detected trees by using street-level and aerial imagery.

This research aims at developing a framework that will apply novel technologies and methods to automate the real-time collection and processing of urban fuel images using artificial intelligence (AI) and computer vision, applied to high-resolution satellite images as well as crowdsensing videos from car-mounted cameras to address previous limitations and provide updated WUI fire risks. This research is performed in multiple stages. First, the satellite images will be analyzed to create automated priority zones around buildings considering topography effects, as well as automatic micro-level fuel mapping through employing convolutional neural networks (CNN). In the next stage, street-level crowdsensing videos from car-mounted cameras will be analyzed to identify the type and characteristics of fuels such as curing of the grass, seasonal changes on deciduous, and the crown base height of conifers. In the final stage, the Fire Behavior Prediction (FBP) and Fire Weather Index (FWI) systems will be implemented to calculate the real-time fire intensity map around buildings. Therefore, the updated fire risk map will help decision-makers in mitigating the risk of fires in WUI areas and increases the resilience of future smart cities. It is worth noting that throughout this report, the results for each step will be presented for the Kinsmen Sport Centre building located in the Edmonton river valley. However, the automated process proposed in this study makes it possible to create similar results for any other building assuming the availability of the necessary data.

2 Satellite Image Analysis

In this section, the automated analysis performed on satellite images is presented. First, topography analysis and priority zone detections are discussed. Then, micro-level fuel detection using satellite images is presented.

2.1 Topographic and Priority Zone Analysis

One of the important factors affecting the fire risk intensity is topography. As the wind blows upward, the flame preheats the fuels located up the hill, causing higher spread levels compared to a flat terrain [1]. This step of the analysis follows the WUI Guideline suggestion in implementing ground slope effects to adjust priority zones around buildings, which will be covered below.

The first step is to extract the topographic information for the entire city of Edmonton using the open-source database CanVec Series managed by the Government of Canada [16]. After finding the elevation data points, the percent ground slope will be calculated as:

$$\% \text{ Ground Slope} = \frac{\text{Elevation}}{\text{Horizontal Ground Distance}} 100 \% \quad (1)$$

Fig. 1 shows the topographic map and the percent ground slope of the area around the Kinsmen Sport Center building. The percent slope is then used to calculate two parameters, the spread factor which scales the rate of spread of the wildfire (m/min) based on how steep the terrain is and will be explained in more detail in the As reported in the preceding sections, the crowdsensing data from car-mounted cameras can overcome major issues facing satellite-based analysis. However, it also has some limitations. For instance, it only can determine fuel characteristics along the road and it cannot cover and extract fuel information inside forested and parkland areas where roads are not available. Thereby, there is a need to integrate the large-scale but low-detailed satellite analysis with the small-scale but high-detailed crowdsensing information to have a more precise updated understanding of the fire risk for WUI areas.

Fire Behavior Analysis section, and the ignition or priority zones which is the area surrounding the building that needs fuel treatment to prevent wildfires from spreading and causing damage into the building [1].

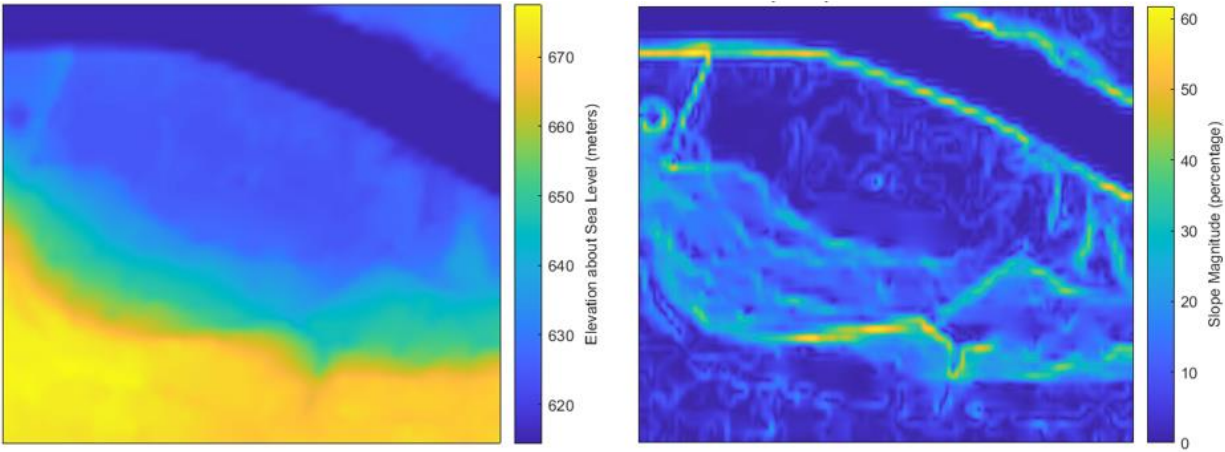


Fig. 1. Topographic map (left) and slope map (right) around the area surrounding the Kinsmen Sport Center building

According to the WUI Guideline [1], the first priority zone extends 0 to 10 meters from the building with the first 1.5 meters being a non-combustible zone. this zone should consist of fire-resistant vegetative combustibles, and potential fuels that cause surface fires, such as mulch and wooden debris, should be removed. In addition, the cured grass should be cut to minimize the probability of ignition and the fire intensity if it were to occur. The second priority zone extends from 10 to 30 meters. In this area, trees should be trimmed, tree branches should be cut at least 2 meters from the ground and separated at least 3 meters from each other while dry grass, debris, and needles should be continuously removed. Finally, the third priority zone extends from 30 to 100 meters and it should contain fire breaks between trees and other potential flammable vegetation.

To find the priority zones, the Open Database of Buildings from Statistics Canada [17] is used to map the buildings of Edmonton and then morphological dilation is performed to generate a buffer around the Kinsmen Sport Centre building to get its respective priority zones as we can see in Fig. 2.



Fig. 2. Priority zones around the Kinsmen Sport Centre building without topographic considerations

The priority zones then need to be adjusted depending on the slope around them since the topography is considered a significant factor in how the fire will spread. According to the WUI Guideline [1], only the second and third priority zone should be adjusted depending on the slope as follows:

- 1) If the slope within the second or the third zone is more than 30% but less or equal to 55%:
 - a. The priority zones should be expanded by a factor of 2 in the downward direction:
 - i. The second zone is extended from 30 to 60 meters.
 - ii. The third zone is extended from 100 to 200 meters.
 - b. The priority zones should be expanded by a factor of 1.5 in the horizontal direction:
 - i. The second zone is extended from 30 to 45 meters.
 - ii. The third zone is extended from 100 to 150 meters.
- 2) If the slope within the second or the third zone is more than 55%:
 - a. The priority zones should be expanded by a factor of 4 in the downward direction:
 - i. The second zone is extended from 30 to 120 meters.

- ii. The third zone is extended from 100 to 400 meters.
- b. The priority zones should be expanded by a factor of 2 in the horizontal direction:
 - i. The second zone is extended from 30 to 60 meters.
 - ii. The third zone is extended from 100 to 200 meters.

Regarding Kinsmen Sport Centre's surrounding region, the areas with slope ranges of 30~55% and above 55% are illustrated in Fig. 3a and Fig. 3b, respectively. Note that the priority zones in this figure do not account for the slope effects.

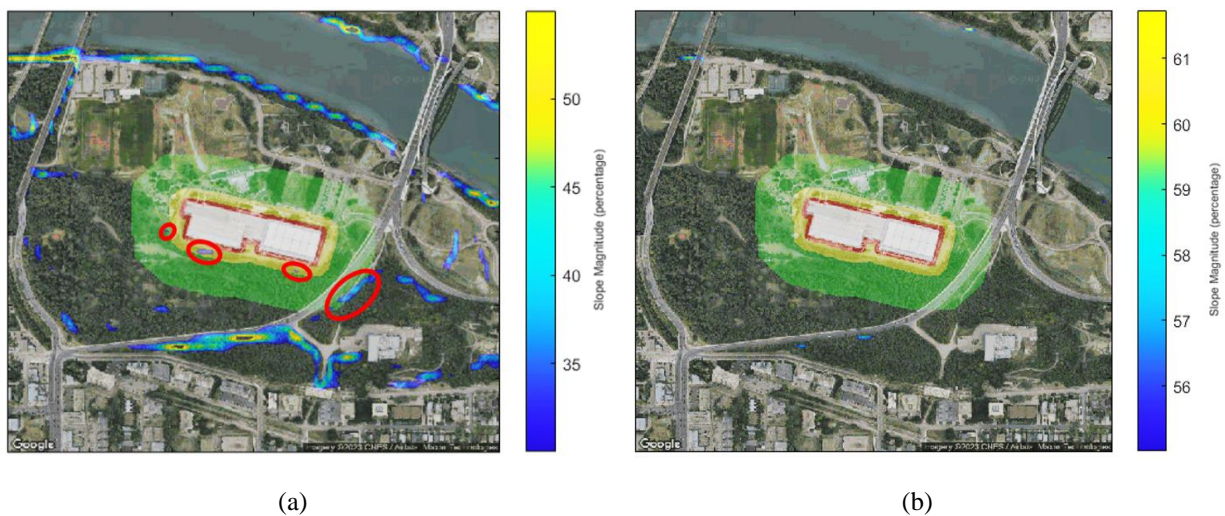


Fig. 3. Areas with slope ranges of (a) within 30% to 55% and (b) above 55% surrounding the Kinsmen Sport Centre building (circled in red represent the slopes inside the priority zones)

As seen in Fig. 3, several regions with slopes greater than 30% but less than 55% are within the second and third priority zones; therefore, we need to extend them by a factor of 2 in the southeast direction and by a factor of 1.5 in the remaining direction as per the rules described in the previous page. This is automatically done by changing the buffer used to create the priority areas. The resulting slope-adjusted priority zones around the Kinsmen Sport Centre building are shown in Fig. 4.



Fig. 4. Slope-adjusted priority zones around the Kinsmen Sport Centre building

2.2 Fuel Identification and Classification

Fuel identification and classification is an important step in identifying several primary characteristics of fire behaviour. The FPB system fuel classification is based on the intrinsic properties of the area such as composition, floor cover, organic layer, stand structure, etc. [18]. In this research, FBP-based fuel types that are commonly found in Edmonton are considered, as seen in Table 1.

The current fuel map used in the Canadian Fire Behavior Prediction (FBP) System, shown in Fig. 5, was derived from forest attribute data based on satellite imagery acquired by NASA sensors, where the fuel types were assigned based on vegetation type, tree species, crown closure, stand height, and other attributes [19]. However, a drawback of this fuel map is that it is on a macro-level scale which is not suitable for urban-scale fire risk analysis. Thus, micro-level fuel mapping needs to be employed for WUI fire risk assessment.

Table 1. Fuel Type and Classification [18]

Fuel Type Name	FBP Label	Description
Deciduous Forest	D-1	The fuel type is composed of moderately trembling aspen, white birch, and balsam poplar trees with medium to tall shrubs and herb layers. They can be leafless due to spring, fall, or disease.
Boreal Spruce Forest	C-2	The fuel type is composed of spruce. It contains continuous shrubs; moderate woody fuels and their tree crowns might extend to the ground which poses a higher risk of crown fires since surface fires can easily spread into them.
Mature Jack Forest	C-3	The fuel type is composed of jack or lodgepoles pine, and their tree crowns are separated from the ground. Sparse conifer understory may be present.
Mixed Wood Forests	M-1/M-2	Fuel type is composed of a mix of conifers and deciduous. The fire behaviour of these fuels will depend on the composition percentage of deciduous/conifers and whether they are leafless (M-1) or with leaf (M-2).
Grass	O1	The fuel type is composed of continuous standing grass. The fire properties of this fuel will depend on the percent of curing or dead and whether is matted like in early spring or standing like in late summer.

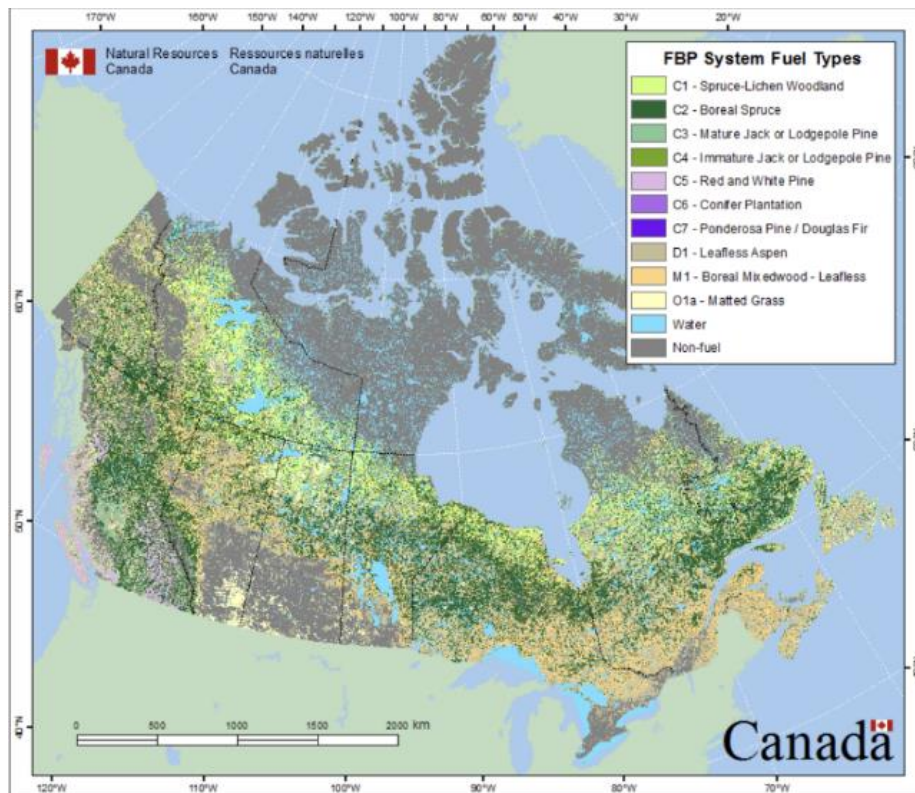


Fig. 5. FBP Fuel Map from the Department of Natural Resources Canada [19]

This step of the research aims at developing an automatic and accurate process that will identify fuels on a micro-level scale according to the FPB system. Previous studies emphasize the use of convolutional neural networks (CNN) to identify wildland fuels in satellite images, such as Alipour et al. [20] which focused on the American fuel system, and Lopez-De-Castro et al. [21] which focused on the Spanish fuel system. However, no similar process was found for the Canadian wildfire system.

A CNN is a type of neural network that is used to process, classify, and identify objects in images. It has a convolutional layer and a significant number of parameters in a neural network that can be adjusted from a “training” dataset. In this research, a ResNet-50 architecture, shown in Fig. 6, is employed to train a model using high-resolution satellite images provided by Maxar Technologies Inc., which are publicly accessible through the Google Maps API. The first step is to extract and label 496 summer satellite images across the Edmonton city region presented in Fig. 7. The assigned pre-labels were grass, trees, and void. Later, more classes will be included according to the FPB fuel system.

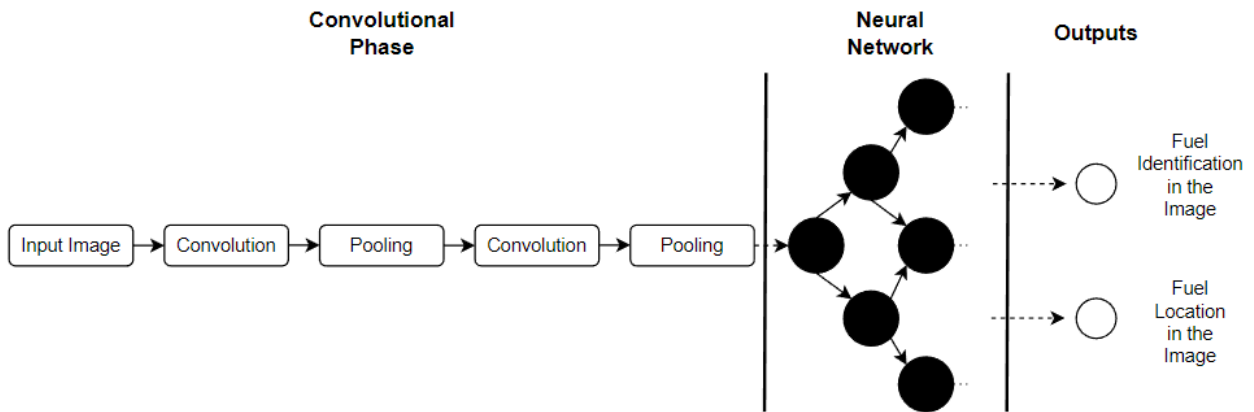


Fig. 6. Simplified Architecture of a Convolutional Neural Network

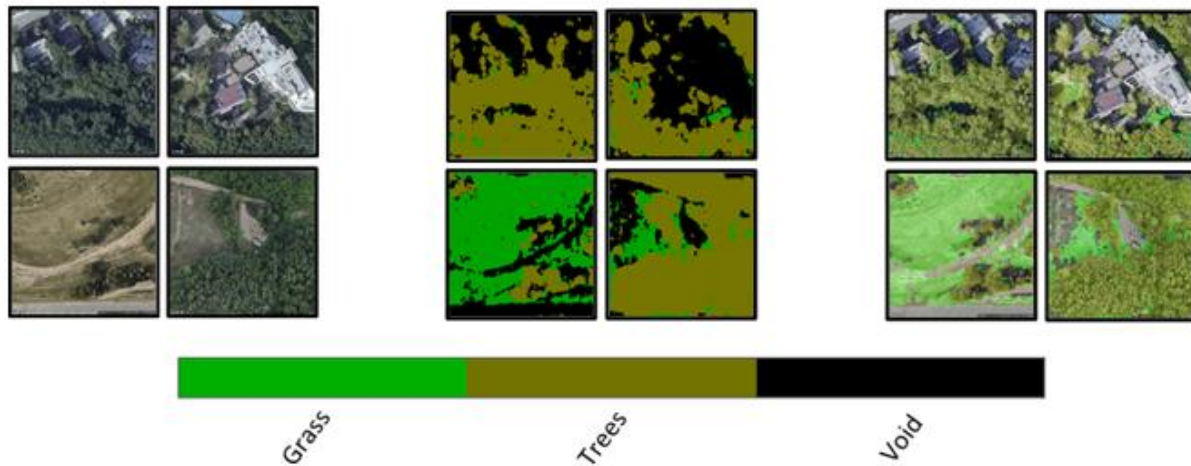


Fig. 7. Summer Satellite Images (Left), Label Masks (Center), and Overlay Maps (Right)

The segmentation process in the summer satellite images achieved a validation accuracy of 93%. However, a limitation of using summer satellite images is that it is hard to differentiate between types of trees, mainly between conifers and deciduous. However, employing winter satellite images will address this major challenge since the conifer foliage are noticeable among leafless deciduous trees. Through training another CNN of ResNet-50 with 80 labeled winter satellite images, shown in Fig. 8, it was possible to identify coniferous areas with a verification accuracy of 82% and a testing accuracy of 72.9%. The deciduous areas would then be detected by subtracting coniferous areas from tree canopies from summer satellite analysis.

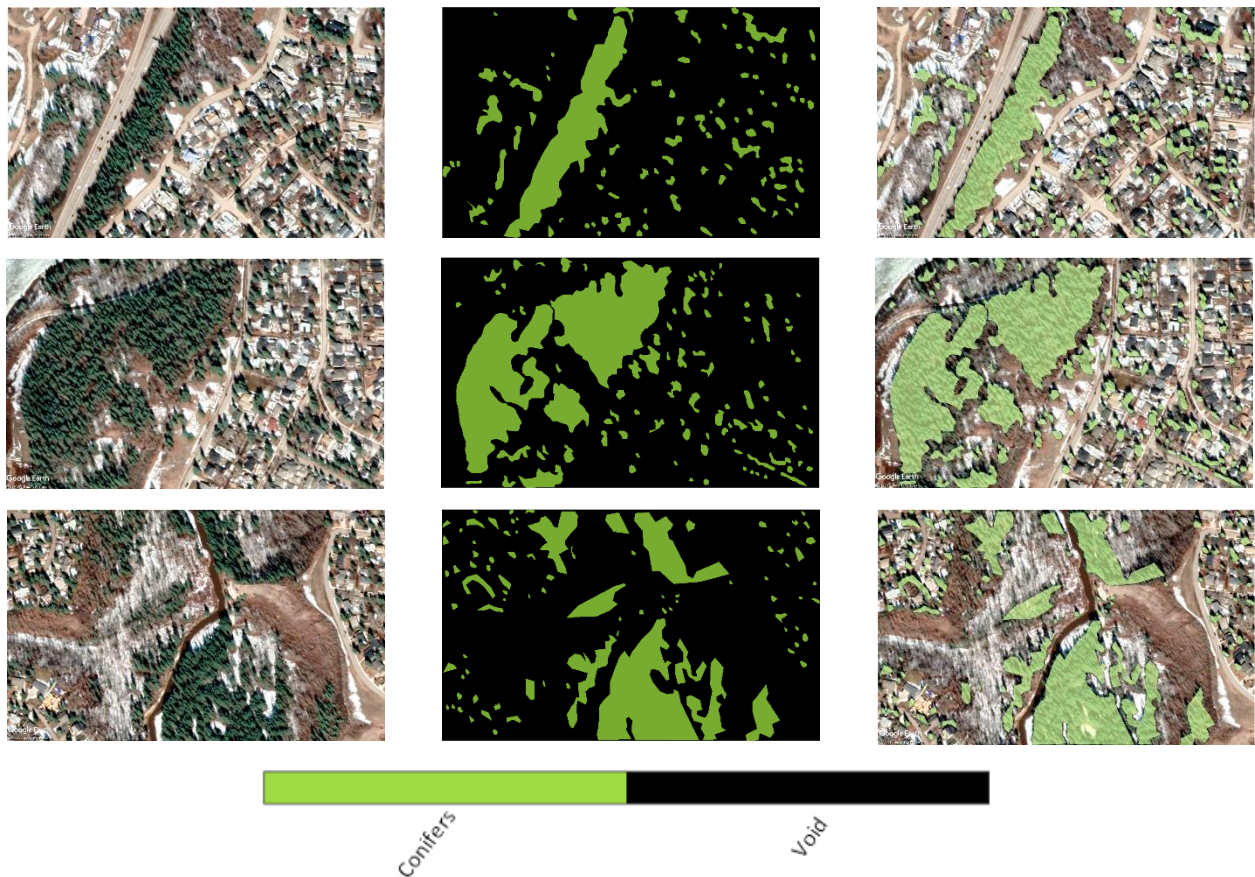


Fig. 8. Winter Satellite Images (Left), Label Masks (Center), and Overlay Maps (Right)

Following the detection of the coniferous, deciduous, and grass-covered areas using the CNN, which combined results are shown in Fig. 9, there is a need to differentiate forests from smaller canopy areas. Forest could be defined using the definition from the Food and Agricultural Organization (FAO) of the United Nations [22] as “land spanning more than 0.5 hectares with trees higher than 5 meters and a canopy cover of more than 10 percent”. Therefore, separated canopy areas detected from CNN will be compared with the minimum forest area to extract forest regions. This process is presented in Fig. 10 for Kinsmen Sport Centre surrounding region.

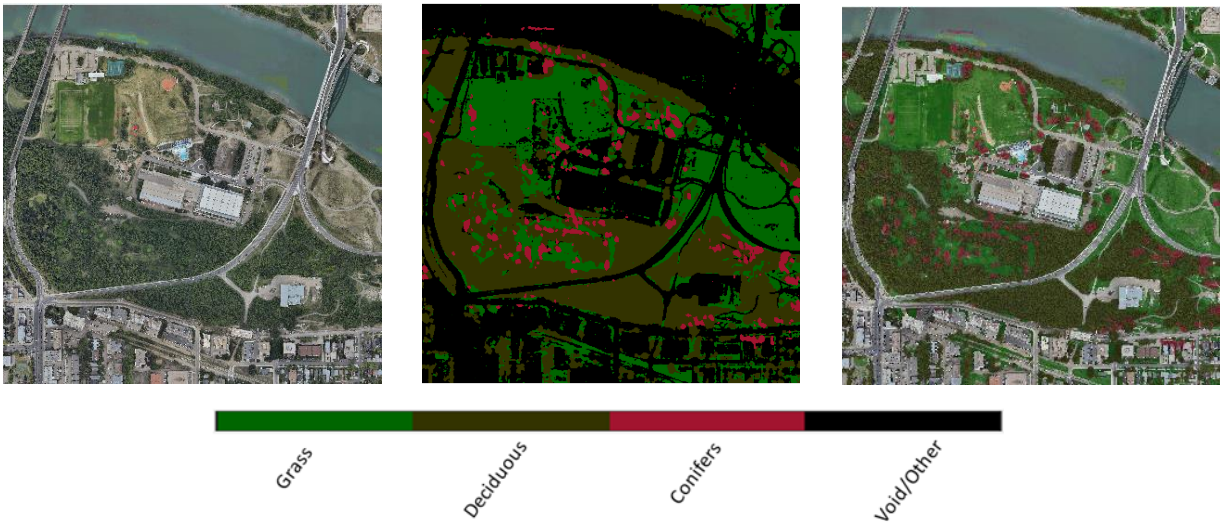


Fig. 9. Satellite Image of Kinsmen Sport Center Building (Left), Label Masks (Center), and Overlay Maps (Right)

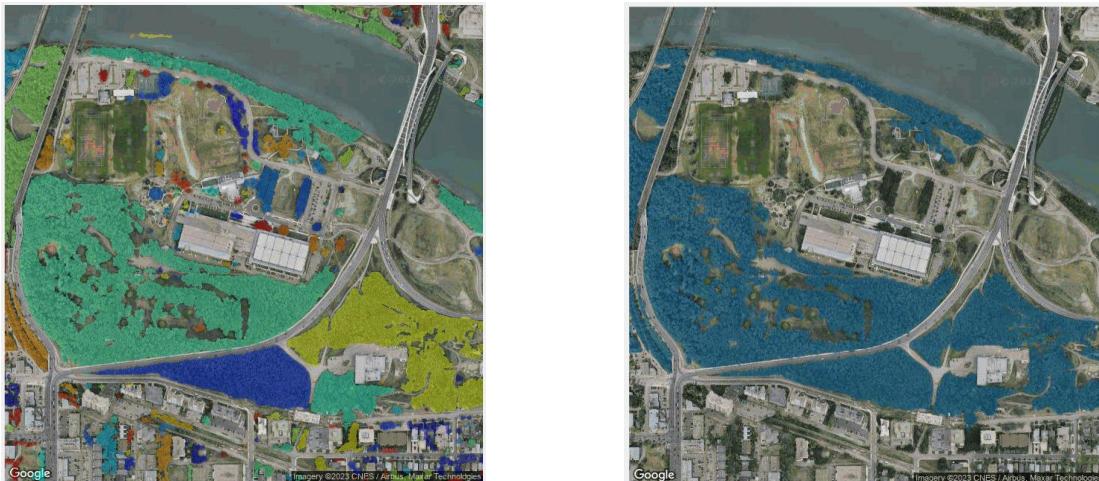


Fig. 10. Isolated canopy areas shown in different colors (left) and areas considered forests (right)

Regarding fuel classes, the composition of each of the forested areas will be compared with the FBP fuel classification. Fig. 11 represents the flowchart of the FBP-based forest fuel classification [23]. It should be noted that in this study, different conifer types such as white and black spruce (C-2) or mature jack and/or lodgepole pines (C-3) are not classified separately for simplicity, which yields a general conifer class (C). Future studies will be dedicated to implementing more fuel types and increasing detection accuracies.

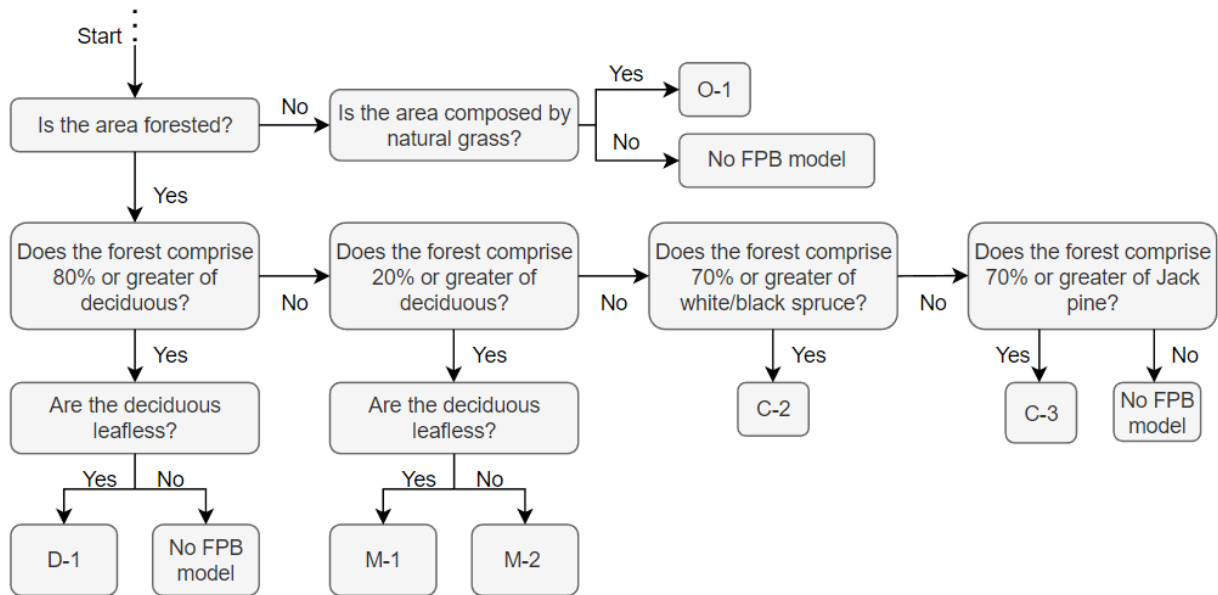


Fig. 11. FBP Classification Flowchart from the Composition of Areas in Alberta [23]

The process of detecting FBP-based fuel classes for the largest forested area in Fig. 10 is shown in Fig. 12. This area was found to be composed of 91.4% deciduous and 8.6% coniferous trees. As a result, according to the diagram in Fig. 11, the region should be classified as FBP type D since the area covered by deciduous trees is greater than 80%. Results corresponding to other forest regions in Fig. 10 for the Kinsmen Sport Centre surrounding area are shown in Table 2. The ID number of each of the forested regions in Table 2 is shown in Fig. 13a and the final FBP classification is illustrated in Fig. 13b.

As a result, since all forested areas were made of more than 80% deciduous trees, they are classified as D1. However, if they were classified as mixed wood, their leafing condition needs to be assigned according to the crowdsensing data to account for M1 and M2 classes. Areas with natural grass are classified as type O.

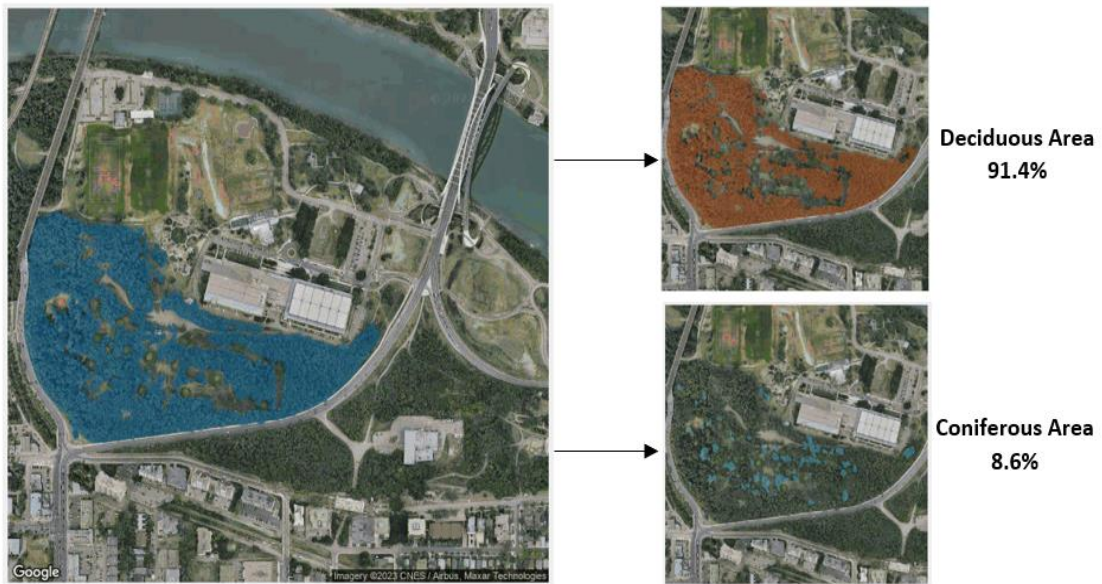


Fig. 12. FBP Classification from the Composition of Forested Areas [23]

Table 2. Composition of Forested Areas around the Kinsmen Building Area.

ID	Deciduous coverage	Conifer coverage	FBP Label
1	96.7%	3.3%	D1
2	92.6%	7.4%	D1
3	91.4%	8.6%	D1
4	86.9%	13.1%	D1
5	99.0%	0.94%	D1
6	87.6%	12.3%	D1
7	89.6%	10.4%	D1

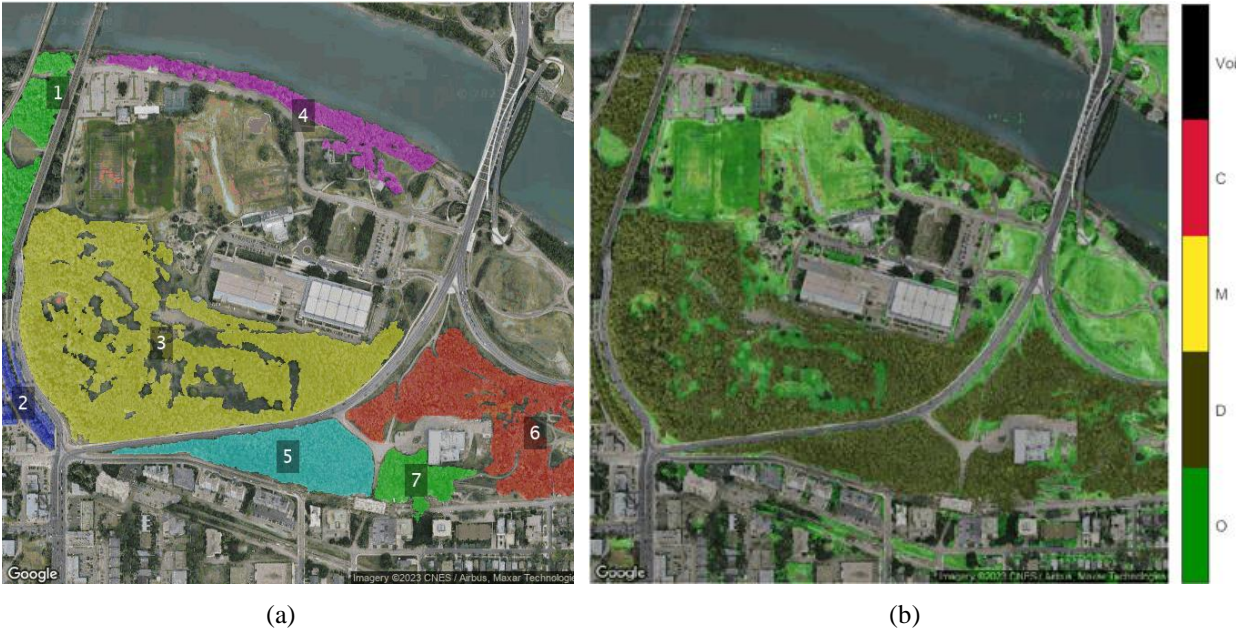


Fig. 13. (a) Labeled Forested Areas and (b) FBP Fuel Map.

3 Street-level Crowdsensing Video Analysis

This section focuses on analyzing the street-level videos recorded from car-mounted cameras. Different fuel types will be detected and their characteristics will be extracted to update fire risk assessments.

3.1 Fuel Identification and Classification

As explained in the Introduction section, there are several limitations regarding identifying fuels using satellite images, such as limitations on the vertical fuel dimensions, seasonal changes such as the leafing of the trees, and the curing of the grass, which are all important characteristic that determines the fire ignition as well as spread risk assessment.

The first step is to implement a computer vision system capable of detecting different types of fuel using GoPro™ car-mounted video cameras. Similar research was done by Azim et al. [24]

in which automatic classification of fuels was done using Google Streetview images based on the American fire behaviour fuel model. However, this research employs real-time videos recorded on car-mounted cameras and extracts fire behaviour properties from the fuels in addition to detecting fuel types.

To train the detection model, 2179 video frames were collected from various areas in Edmonton, followed by labeling objects of interest, including conifers, deciduous (leafless or with leaf), and shrubs. A sample label is shown in Fig. 14 using the LabelMe software. Thereafter, the labeled data were augmented and employed to train a CNN capable of identifying the fuels of interest. The verification accuracy was reported as 90%. Subsequently, in order to prevent multiple detections of a single object, an algorithm known as Simple Online and Realtime Tracking (SORT) [25] is employed, which uses a Kalman filter to predict object movements across frames. Fig. 15 presents prediction samples of different fuel identifications inside street-level video frames.

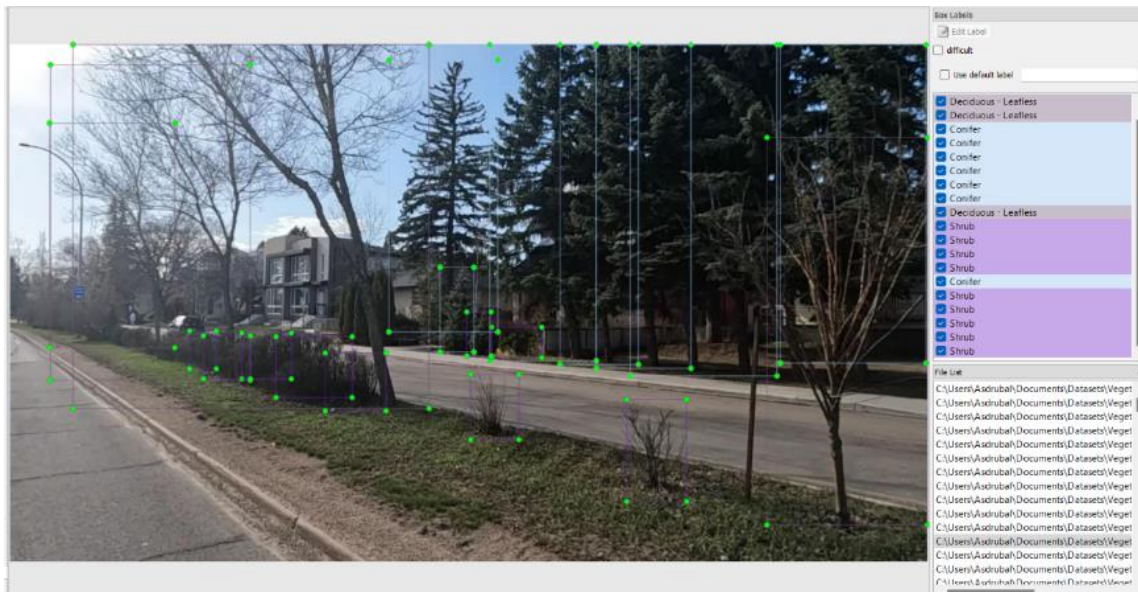


Fig. 14. Labelling Vegetation in Car Mounted Videos.

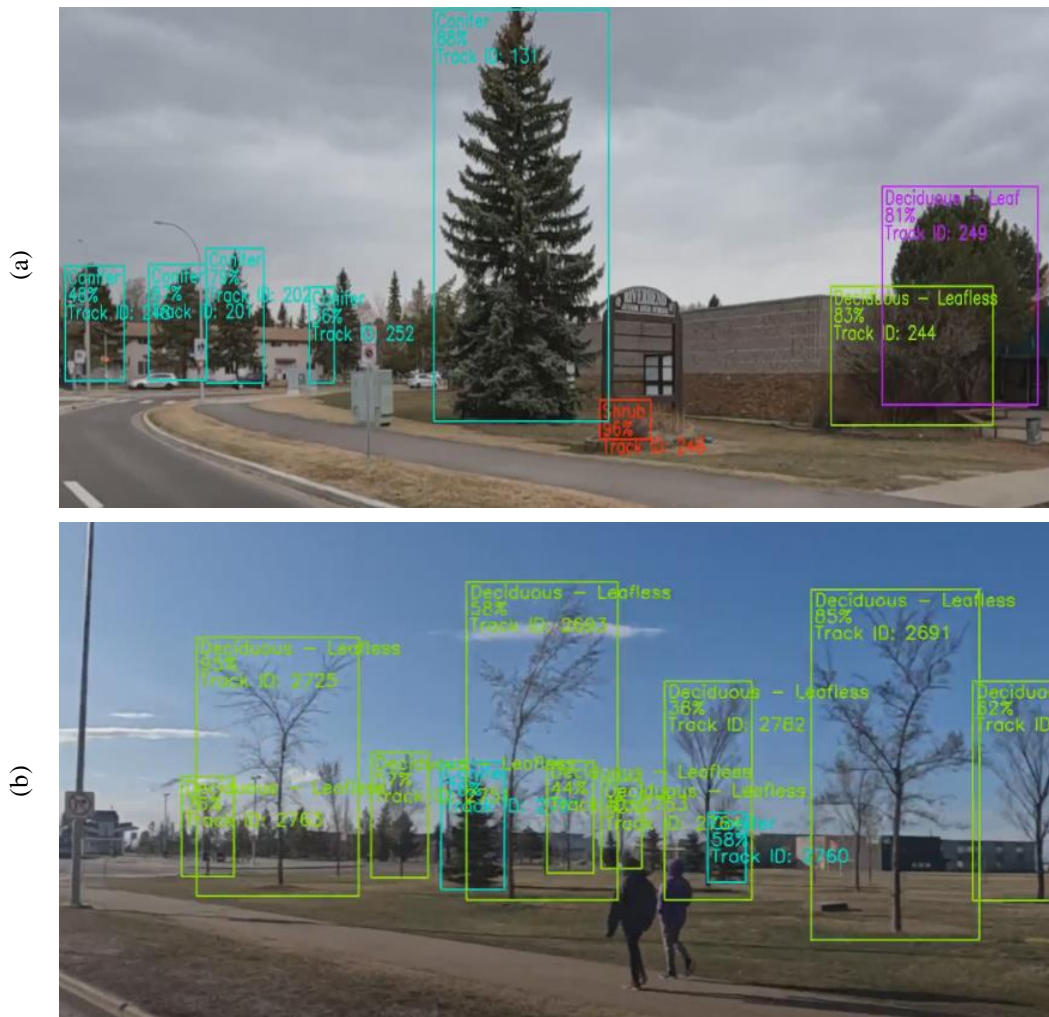


Fig. 15. Samples of fuel identification predictions from the CNN Model for (a) conifer and (b) deciduous trees

3.2 Crown Base Height Estimation

This section aims at one of the important characteristics of conifer trees. Crown base height (CBH) is defined as the distance between the ground and the base of the crown, shown in Fig. 16. A fire has a higher rate of spread if the CBH is low since surface fires due to dry grass, debris, or horizontal slash have a direct path to the conifer crowns [26]. As such, pruning is usually necessary

for high-risk areas to keep CBH within the safe range (around 2 meters or more) and reduce the risk of crown fires [26].

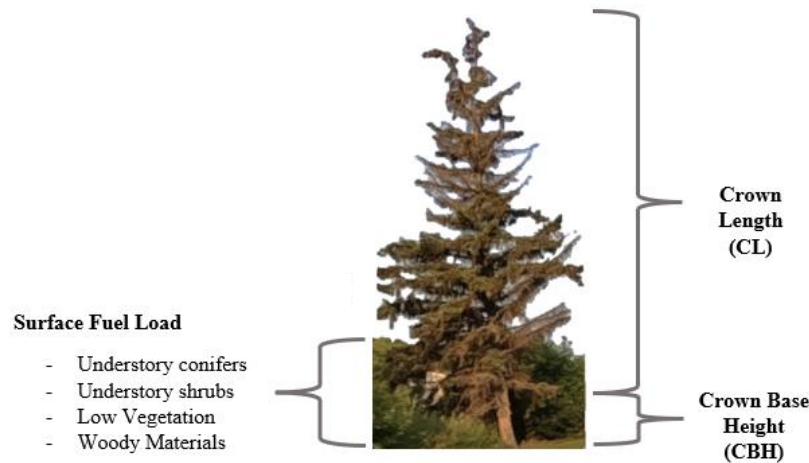


Fig. 16. Fuel Characteristics of Conifers (Beverly, 2020) [26]

The objective of this section is to estimate the height of conifers using global navigation satellite systems (GNSS) embedded in the GoPro™ cameras. Due to perspective distortion, the object looks smaller from a longer distance, and vice versa. Considering a car traveling along the road, this phenomenon can be employed to estimate the dimensions of the objects from car-mounted video frames, which process is shown in Fig. 17. Considering the error in the GPS sensor of the camera, this research only considered detections acquired in a straight path travel of the car. The algorithm that was used to filter out detections obtained around a curve is based on the Ramer–Douglas–Peucker algorithm to approximate straight lines [27].

In order to find the height and the location of the tree, the camera is assumed to be positioned at an ideally vertical plane, on which the object is located. By having two frames captured from an object and knowing the distance the vehicle has traveled between the two frames (Δx), employing similar triangles theorem yields the distance of the object from the vehicle, according to Fig. 18 and Eq. (2).

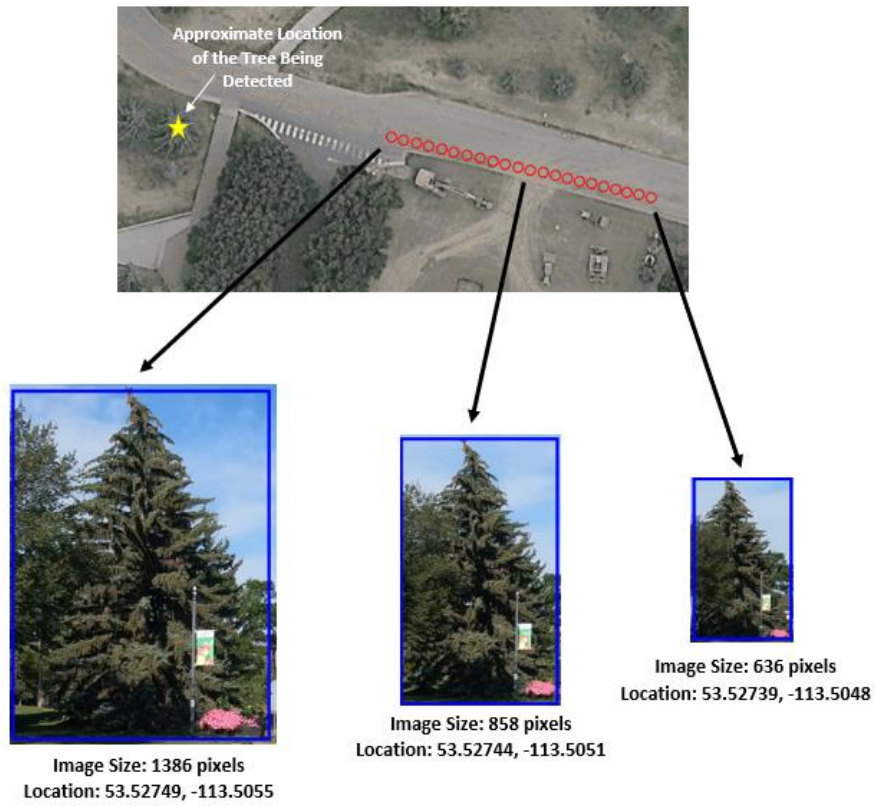


Fig. 17. Conifer Image Size Increase as The Camera Gets Closer

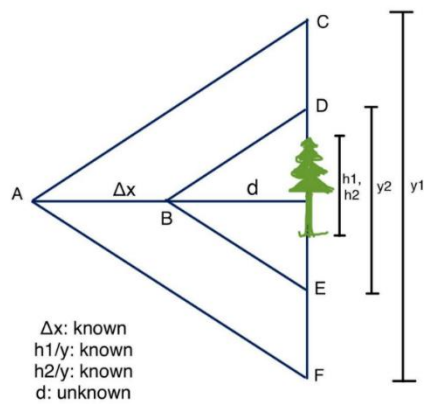


Fig. 18. Representation of the geometry when two frames are captured (as the vehicle moves from point A to B)

$$\frac{d}{d+\Delta x} = \frac{y_2}{y_1} = \frac{\frac{h}{y_1}}{\frac{h}{y_2}} = \frac{\frac{h_1}{h_f}}{\frac{h_2}{h_f}} = \frac{h_1}{h_2} \quad (2)$$

In Eq. (2), d is the horizontal distance of the vehicle from the object in the second position, h_1 and h_2 are the pixel count of the object height inside the first frame and second frame, respectively, and h_f is the pixel count of the total height of the frame, which is constant. By simplifying the equation, we reach Eq. (3):

$$d = \frac{\Delta x}{\frac{h_2}{h_1} - 1} \quad (3)$$

After estimating the horizontal distance, the height of the object can be determined according to Fig. 19 and Eq. (4), which represent the relationship between the vertical field of view (FOV) of the camera and the height of the object.

$$height = 2 \tan\left(\frac{FOV}{2}\right) \times d \times \frac{h_2}{h_f} \quad (4)$$

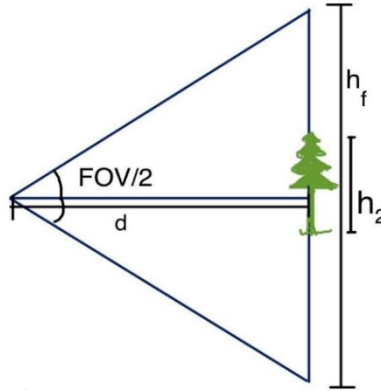


Fig. 19. Representation of the geometry for the second frame

Regarding the conifer tree in Fig. 17, the diagram in Fig. 20 shows multiple detections of the same tree across multiple video frames (blue dots). Ideally, they should follow a linear pattern. However, due to small operational errors, modifications need to be applied in order to estimate the linear function. Therefore, the best line is fitted by minimizing the mean squared error, seen in Fig. 20.

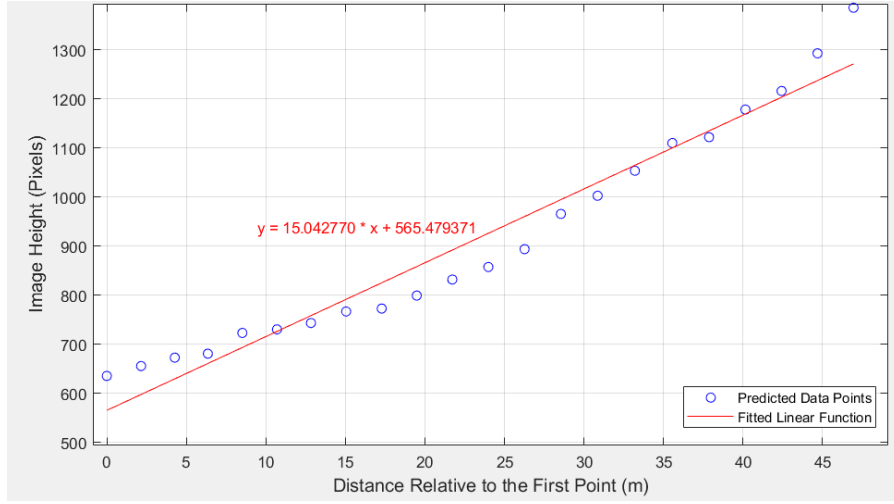


Fig. 20. Height-Distance Relationship of the Conifer Detected Above. Blue Dots are The Predictions by the CNN and Red Line is a Fitted Linear Function

In order to calculate the tree height, assuming point A at the start point where $x_A = 0$, and B at the endpoint where $x_B = 46.9$, the height in pixels h_1 and h_2 will be:

$$h_1 = 15.043 \times 0 + 565.479 = 565 \text{ pixels} \quad (5)$$

$$h_2 = 15.043 \times 46.9 + 565.479 = 1272 \text{ pixels} \quad (6)$$

Thereby, the distance from point B and the real height of the conifer is:

$$d = \frac{\Delta x}{\frac{h_2}{h_1} - 1} = \frac{46.9 - 0}{\frac{1272}{565} - 1} m = 37.48 m \quad (7)$$

$$\text{height} = 2 \tan\left(\frac{FOV}{2}\right) \times d \times \frac{h_2}{h_f} = 2 \tan\left(\frac{71^\circ}{2}\right) \times 37.48 \times \frac{1272}{2992} = 22.73 m \quad (8)$$

Hence, the height of the conifer is estimated at 22.7 meters. Several height detections of other conifers were performed around and the errors of the distance and height estimation were 5.4% and 4.6% respectively.

Following the height estimation, an additional neural network is trained to estimate the CBH and CL with 224 images, as shown in Fig. 21, where below the red line was labeled as CBH and above the line was labeled as CL. Therefore, for the example shown before in Fig. 17, the

CBH and the CL of the conifer were estimated to be at 6.8% and 93.2% of its total height (22.7 m), respectively, as illustrated in Fig. 22.

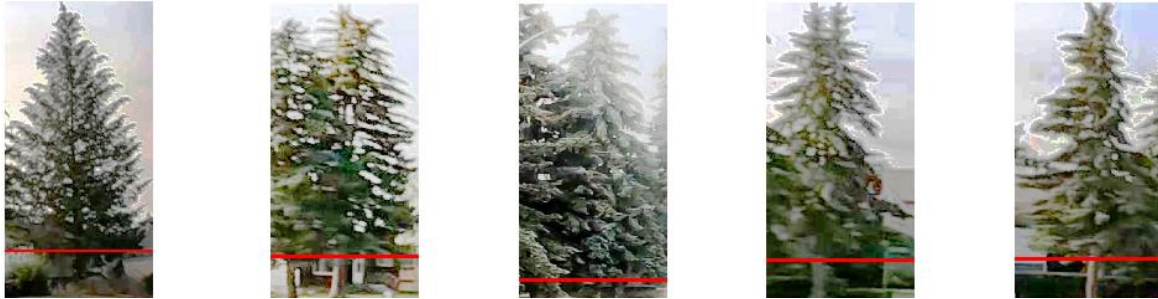


Fig. 21. Conifer Dataset to Estimate the CBH and CL

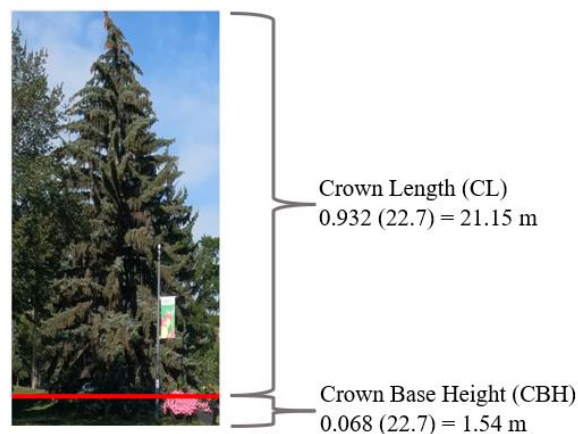


Fig. 22. Neural Network Estimation for CBH and CL

3.3 Grassland Curing Assessment

One of the parameters used to measure the Rate of Spread in accordance with the FBP system is the type of grass fuel. The currently available fire behaviour data for grass fuel type in Canada is limited. A grass-fire hazard index was developed in 1938 by Wright [28], but it was based on small test fires, for which no quantitative rates of spread were recorded. To estimate the spread rate for fuel type O-1, which represents grass fuel, regression functions derived from Australian grass fire

data were used. Data were available for tall grass and short grass, with the tall grass being representative of midsummer fields of dry grass and the cut grass of early spring grass fuel matted down by snow loads.

The percentage of cured or the proportional number of grass stems that have dried out and are no longer green and growing is considered to have a significant influence on grassland fire behaviour. In the absence of definitive research on this subject, a simple linear relationship was adopted based on the understanding that fire spread in grassland is unlikely when the degree of curing is less than 50%. The rate of fire spread in grasslands varies roughly in proportion to the percentage of cured or dead material. To account for the degree of curing, an equation from the FBP system is used to adjust the rate of spread for grass fuel when the degree of curing is less than 100%, as provided below:

$$CF = 0.02 \times C - 1.0 \quad C > 50 \quad (9)$$

where CF is the grass curing coefficient and C is the degree of curing (%). However, when C is less than 50%, then the curing coefficient becomes zero. This curing coefficient is an important factor that determines the rate of spread for grass and will be discussed more in detail in the Fire Behavior Analysis section.

To account for the grass curing evaluation, updated data from crowdsensing sources is needed. The satellite data is not reliable as they are not updated regularly. The videos taken from crowdsensing are extracted into frames in order to be analyzed. DeepLab semantic scene segmentation model [29] was employed to segment the grass-terrain areas. The pixel coordinates of the segmented area are then collected for further analysis. As shown in Fig. 23, the grass field from the extracted frame is segmented and shown by a red-colored area.



Fig. 23. Extracted frame from crowdsensing data (right), segmented grass field (left)

In order to assess the curing percentage of grasslands, colour analysis is required. Therefore, the coordinates of each segmented pixel along its corresponding color components in red, green, and blue (RGB) channels are recorded. To account for the errors and variations, normal distributions are fitted to different RGB color channels, as presented in Fig. 24. Then, the mean value of the fitted distributions will be extracted to estimate the most probable color outcome of the grass region inside the image. In the next step, the hue colour system is employed for a more intuitive way of understanding color relationships.

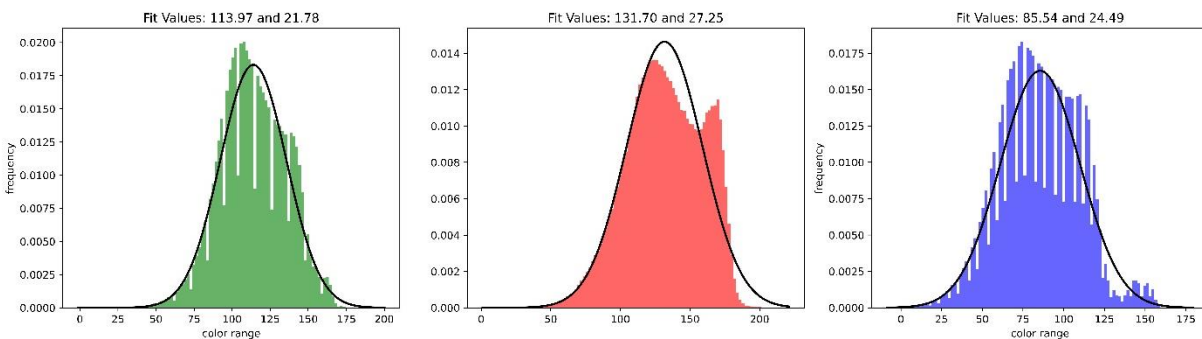


Fig. 24. Normal distribution of RGB colour range for the grassland area

The HVS colour wheel is a fundamental tool for understanding and working with colour in many fields, including art, design, and science. It is a circular diagram that organizes colours based on their hue value, which is determined by the wavelength of light that the colour reflects. The wheel typically includes 12 segments, each representing a different hue. The hues are arranged in a

circular order and often start with red, followed by orange, yellow, green, blue, and purple. The wheel can be expanded to include intermediate hues between these primary hues, resulting in a more nuanced colour spectrum. To extract the hue value from an RGB colour, you can use an RGB to HSV conversion formula. These formulas calculate the hue angle of the color on the color wheel, which ranges from 0 to 360 degrees. The resulting hue value can then be used to identify the color and its position on the hue color wheel. A representation of the hue color wheel is shown in Fig. 25.

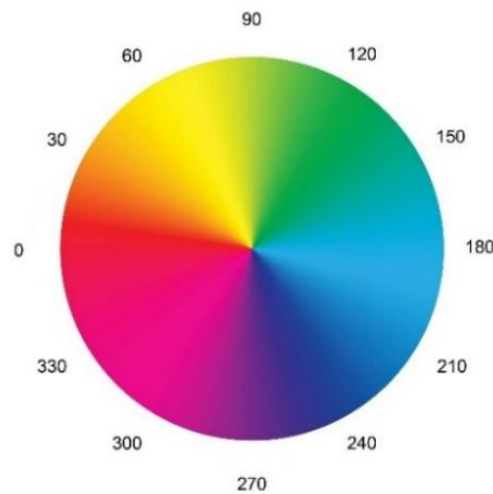













Fig. 25. Hue color wheel

Table 3 presents a description of the curing of grasses in south-eastern Australia and the associated physiological changes according to the Australian Grassland Curing Guide [30]. In order to extract color representations for each curing range, RGB values have been extracted from corresponding images of each curing condition, which are presented in Table 4. The RGB values are subsequently converted into hue values, which are compared to the average hue value obtained from the colour analysis of segmented photos from street-level crowdsensing video frames.

Table 3. Grass Curing Characteristics according to the Australian Grassland Curing Guide [30]

Phase	% Cured	Grass colour	Landscape Features
Green	0	Green	The landscape is entirely green, with no seed heads visible
	10	Green	The landscape is entirely green with seed heads visible
	20	Green-Yellow	Seed heads change colour
	30	Green-Yellow	Yellowing becoming apparent in leaves
Yellow	40	Yellow-Green	Green, with yellowing a significant part of the landscape
	50	Yellow-Green	The landscape is half-green and half yellow
	60	Yellow-Green	Yellow, with green a significant part of the landscape
Dry	70	Yellow-Straw	A minor amount of green or greenish-yellow visible
	80	Yellow-Straw	Non-significant amount of green or greenish-yellow visible
	90	Straw	Very little green showing anywhere
	100	Bleached	No green anywhere in the landscape

Table 4. RGB ranges corresponding to curing percentages according to the Australian Grassland Curing Guide [30]

Color	RGB	Curing	Color	RGB	Curing
	RGB: (49, 96, 51)	0%		RGB: (195, 130, 36)	60%
	RGB: (68, 119, 65)	10%		RGB: (206, 144, 41)	70%
	RGB: (89, 149, 74)	20%		RGB: (217, 175, 71)	80%
	RGB: (128, 177, 69)	30%		RGB: (227, 192, 96)	90%
	RGB: (151, 193, 75)	40%		RGB: (247, 210, 119)	100%
	RGB: (198, 204, 81)	50%			

As reported in the preceding sections, the crowdsensing data from car-mounted cameras can overcome major issues facing satellite-based analysis. However, it also has some limitations.

For instance, it only can determine fuel characteristics along the road and it cannot cover and extract fuel information inside forested and parkland areas where roads are not available. Thereby, there is a need to integrate the large-scale but low-detailed satellite analysis with the small-scale but high-detailed crowdsensing information to have a more precise updated understanding of the fire risk for WUI areas.

4 Fire Behavior Analysis

In this section, the focus is on integrating the extracted information from previous stages of satellite- and crowdsensing-based analyses toward a more accurate and updated fire risk mapping. The current Canadian fire model system is built upon two main components, the Fire Weather Index (FWI) [17] and the Fire Behavior Prediction (FBP) [16]. The FBP was developed in 1982 by Van Wagner and outputs a range of fire behaviour characteristics such as the Rate of Spread (ROS) and the Head Fire Intensity (HFI). ROS is the number of meters consumed by the fire per minute (m/min) while HFI is the amount of energy released per meter progress of the fire front line per second and is often reported in kW/m. In this report, these parameters are calculated for the Kinsmen Sport Centre building on two different dates, August 16th and November 1st in 2022, to have a better comparison of the changes due to weather and fuel conditions.

4.1 Rate of Spread

According to the FBP system, ROS depends on the Initial Spread Index (ISI) and constants (a , b , and c) that are related specifically for each type of fuel, calculated as:

$$ROS = a \times (1 - e^{-b \times ISI})^c \quad (10)$$

Since the fuel detection using satellite images yields deciduous forest D-1 and grass O, the corresponding constant values are provided in Table 5.

Table 5. Rate of Spread Constant for Fuels of Interest [16]

Fuel Type	<i>a</i>	<i>b</i>	<i>c</i>
D-1 (deciduous leafless)	30	0.0232	1.6
O-1a (matted grass)	190	0.0310	1.4
O-1b (fully cured)	250	0.0350	1.7

To find the ISI, a set of equations and procedures are used, the starting point of which is to find the Fine Fuel Moisture Content (FFMC). FFMC is a unitless numerical rating of the moisture content of litter and other cured fine fuels and relates to how flammable these are [18]. The higher the FFMC, the higher the probability of ignition. The FFMC is determined by following the FWI handbook (Appendix A) procedure where several weather conditions are used as inputs such as relative humidity, temperature, rainfall, and wind [17]. These weather data can be obtained from weather stations. Meanwhile, the FFMC can be extracted from the Fire Weather Maps managed by Natural Resources Canada [18]. Regarding the target dates in this report, the maximum FFMC for August 16th and November 1st of 2022 were found as 91 and 84, respectively. Following the FFMC, Initial Spread Index with Zero Wind (ISZ) will be extracted from the FWI handbook [17], presented in Table 6. Therefore, the ISZ on August 16th and November 1st of 2022 were 5 and 2, respectively [17].

Table 6. Relationship of the FFMC and the ISZ according to the FWI Handbook [17]

FFMC	0~32	33~37	38~42	43~47	48~52	53~57	58~62	63~67	68~72	73~77	78~79	80	81	82	83	84
ISZ	0	0	0	0	0	0.5	0.5	0.5	0.5	1	1	1	1.5	1.5	1.5	2
FFMC	85	86	87	88	89	90	91	92	93	94	95	96	97	98	99	
ISZ	2	2.5	3	3	4	4	5	6	7	8	9	10	11	13	15	

Once the Initial Spread Index with Zero Wind is obtained, then the Rate of Spread with Zero Wind will be calculated through the following equations that are characteristically unique for each fuel [18]:

$$RSZ_{D-1} = 30 \times (1 - e^{-0.0232 \times ISZ})^{1.6} \quad (11)$$

$$RSZ_{O-1a} = 190 \times (1 - e^{-0.0310 \times ISZ})^{1.4} \times CF \quad (12)$$

$$RSZ_{O-1b} = 250 \times (1 - e^{-0.0350 \times ISZ})^{1.7} \times CF \quad (13)$$

where CF is the curing factor of the grass found in the Grassland Curing Assessment section. After assigning the RSZ value for each fuel that was identified from the satellite images in Fig. 13b, the slope-adjusted zero-wind rate of spread (RSF) can be calculated through the following equation [18]:

$$RSF = RSZ \times SF \quad (14)$$

where SF is the spread factor calculated as a function of the slope of the terrain, as below [18]:

$$SF = e^{3.533 \times \left(\frac{\text{Ground Slope}}{100}\right)^{1.2}} \quad (15)$$

The variation of the spread factor for the Kinsmen Sport Centre area is shown in Fig. 26.

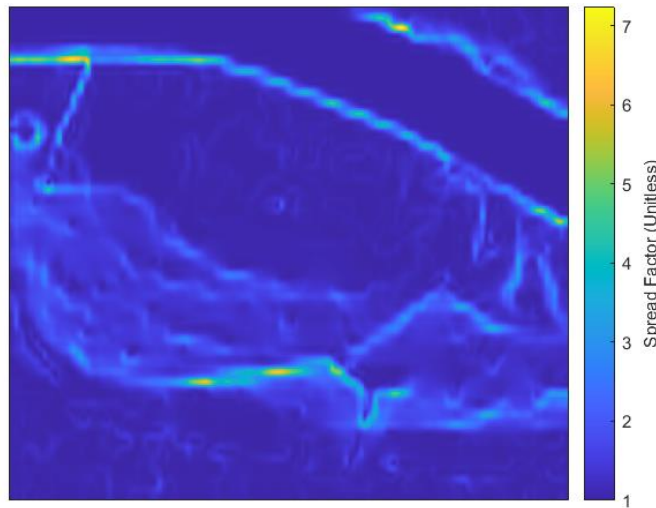


Fig. 26. Spread Factor for the Kinsmen Area

Following RSF calculation, the slope-adjusted zero-wind initial spread index (ISF) will be calculated through the following equations [18] that are specific for each of the fuels. Eq. (16) is proposed for grass classes of O-1a and O-1b, while Eq. (17) represents other fuel classes.

$$ISF = \frac{\ln\left(1 - \left(\frac{RSF}{CF \times a}\right)^{\frac{1}{c}}\right)}{-b} \quad (16)$$

$$ISF = \frac{\ln\left(1 - \left(\frac{RSF}{a}\right)^{\frac{1}{c}}\right)}{-b} \quad (17)$$

Then, the slope wind speed equivalent (WSE) from ISF, defined as the effect of the percent slope on the rate of spread if it were a wind speed [18], will be calculated. This parameter is a function of the FFMC as seen in the equation below [18]:

$$WSE = \frac{\ln\left(\frac{ISF}{0.208 \times f(F)}\right)}{0.05039} \quad (18)$$

where $f(F)$ is the FFMC function for the initial rate of spread calculated as [18]:

$$f(F) = 91.9 \times e^{-0.1386 \times m} \times \left[1 + \frac{m^{5.31}}{4.93 \times 10^7}\right] \quad (19)$$

and “ m ” is defined as [18]:

$$m = \frac{147.2 \times (101 - FFMC)}{59.5 + FFMC} \quad (20)$$

In the next step, the actual wind will be included as a vector summation in the x and y-axis using the following equations [18]:

$$WSX = [WS \times \sin(WAZ)] + [WSE \times \sin(SAZ)] \quad (21)$$

$$WSY = [WS \times \cos(WAZ)] + [WSE \times \cos(SAZ)] \quad (22)$$

$$WSV = \sqrt{(WSX)^2 + (WSY)^2} \quad (23)$$

where WS is the current wind speed, WAZ is the current wind azimuth, and SAZ is the uphill slope azimuth. Following the calculation of the net effective wind speed (WSV) in Eq. (23), the wind speed function ($f(W)$) will be calculated through Eq. (24) [18]:

$$f(W) = e^{0.05039 \times WSV} \quad (24)$$

Then, the actual rate of spread is determined using the wind speed equivalent function in Eq. (24) and the fine foliar moisture function in Eq. (19) through the following equation [18]:

$$ISI = 0.208 \times f(W) \times f(F) \quad (25)$$

Finally, the ISI will be converted back to the rate of spread through Eqs. (11)-(13) to get the slope and wind-adjusted rate of fire spread indices measured in meters per minute [18]:

$$RSI_{D-1} = 30 \times (1 - e^{-0.0232 \times ISI})^{1.6} \quad (26)$$

$$RSI_{O-1a} = 190 \times (1 - e^{-0.0310 \times ISI})^{1.4} \times CF \quad (27)$$

$$RSI_{O-1b} = 250 \times (1 - e^{-0.0350 \times ISI})^{1.7} \times CF \quad (28)$$

Fig. 27 shows the rate of spread for August 16th and November 1st, respectively. The average rate of spread for August 16th was 1.54 m/min with a maximum value of 5.36 m/min in the regions with higher percent slope, while the average and maximum rate of spread for November 1st were 1.46 and 11.12 m/min, respectively. The average rate of spread on August 16th was higher than in November due to the higher Fine Foliar Moisture Content (FFMC) value.

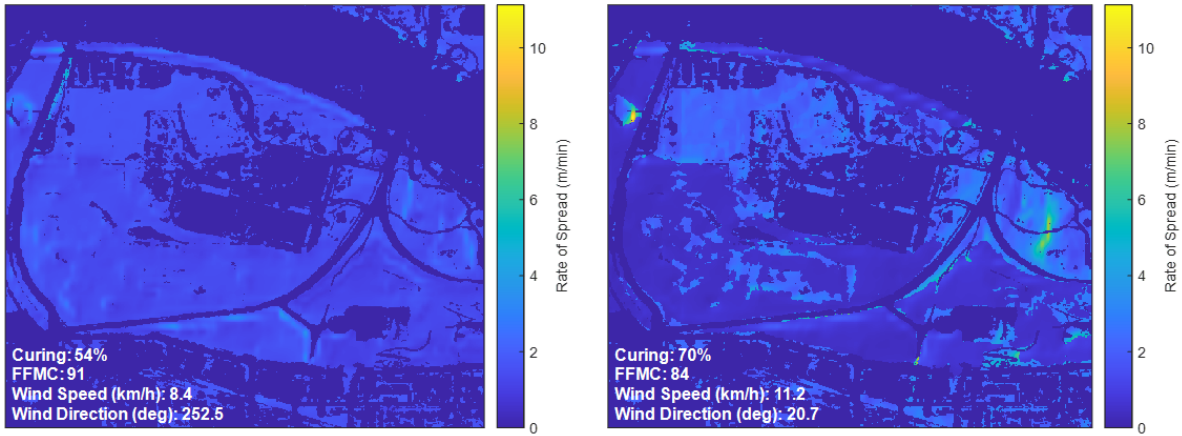


Fig. 27. Overall Rate of Spread for August 16th (Left) and November 1st (Right)

A higher FFMC means that weather factors such as relative humidity and temperature facilitate a higher probability of fire ignition. On the other hand, some regions on November 1st had a higher rate of spread because of the higher levels of grass curing as well as the higher magnitude of the

wind speed, which can potentially lead to a higher chance of surface fires. As a result, it can be concluded that updated information from integrating street-level crowdsensing videos with satellite analysis provides more insights toward parameters affecting fire risks in urban regions.

4.2 Head Fire Intensity

Following the findings of the rate of spread, the head fire intensity (HFI), defined as the amount of energy released per meter progress of the fire front line per second, will be calculated as one of the crucial parameters employed in fire risk assessments. The equation used to compute this parameter is known as Byram's Fire Intensity Equation and is defined in the FBP system [18] as:

$$HFI = 300 \times TFC \times ROS \quad (29)$$

where 300 KJ/Kg is the heat of combustion, TFC is the total fuel consumption and is equal to the surface fuel consumption (SFC) plus the crown fuel consumption (CFC), and ROS is the overall rate of spread calculated in the previous section.

The FBP system [18] approximates the SFC for grass to be 0.3 kg/m². To compute the SFC for deciduous, it is necessary to find the buildup index (BUI) which can be obtained by inputting the relative humidity and temperature into a lookup table from the fire weather index (FWI) system [17]. The SFC for different fuel types is then determined through the following equations:

$$SFC_{D-1} = 1.5 \times [1 - e^{-0.0201 \times BUI}] \text{ kg/m}^2 \quad (30)$$

$$SFC_{O-1} = 0.3 \text{ kg/m}^2 \quad (31)$$

Following the calculation of SFC the grass and deciduous classes, Byram's fire intensity in Eq. (29) is employed to find the HFI for both August 16th and November 1st. The variations of HFI in each of the priority zones, previously shown in Fig. 4, are illustrated in Fig. 28 for the two dates of August 16th and November 1st. In addition, key statistics of the HFI values per zone on each date are presented in Table 7. As expected, the regions located in the southeast of the building, where there is a higher percent slope and higher crown fuel, have higher fire intensity.

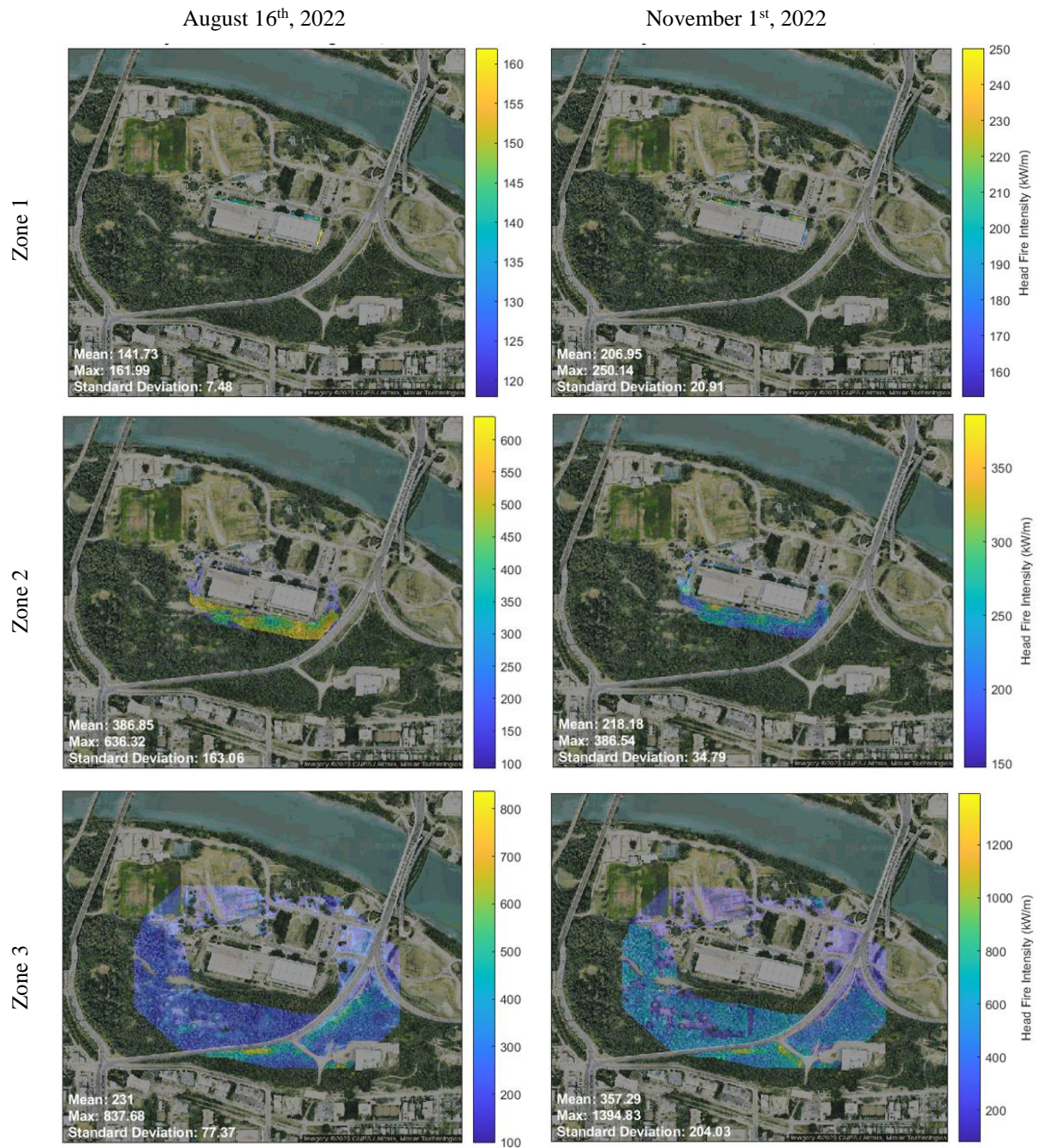


Fig. 28. Fire Intensity in each priority zone for August 16th and November 1st

Table 7. Head Fire Intensity Results for the Kinsmen Building Area

Date	Zone	Mean [kW/m]	Max [kW/m]	Max Intensity Location
August 16 th , 2022	1	141.73	161.99	[53.52566, -113.50520]
	2	386.85	636.32	[53.52592, -113.50826]
	3	231.00	837.68	[53.52428, -113.50544]
November 1 st , 2022	1	206.95	250.14	[53.52578, -113.50636]
	2	218.18	386.54	[53.52584, -113.50778]
	3	357.29	1394.83	[53.52422, -113.50684]

HFI is directly related to the flame length, thus it can be used to classify fire intensities. According to the National Wildfire Coordination Group (NCWG) website [31], Table 8 can be used to rate the fire intensity class from the FBP outputs. Many studies have been conducted to relate fire intensity and flame length to fire hazards. For instance, a study by Oregon State University [32] has related fire intensity to the susceptibility (damage expectancy) in wildland regions. In future studies, such relations can be investigated for urban areas.

Table 8. The flame length and intensity class corresponding to each threshold of fire intensity [31]

Intensity Class	Flame Length (ft)	Fire Intensity Thresholds (kW/m)
1	< 1	< 10
2	< 4	< 500
3	< 8	< 2000
4	< 12	< 4000
5	< 18	< 10000
6	> 18	> 10000

5 Graphical User Interface

This section demonstrates the demonstration (demo) version of a web-based Graphical User Interface (GUI) to present the outputs of this research. This GUI is publicly accessible through the web address: <https://uofa-combine-project.github.io/WUI-Fire-Risk-Assessment/>. According to the available data presented in the previous sections, the current demo version works for the Kinsmen Sport Centre building, showing fuel results as well as fire behavior parameters for two specific dates on August 16th and November 1st, 2022. However, the overall features of the GUI are developed to be applicable for any building of interest in Edmonton in the future considering crowdsensing data availability.

The user flow diagram for the proposed GUI is illustrated in Fig. 29. After entering the GUI through the landing page, shown in Fig. 31, users can select their building of interest through clicking on the building location on the map, noting that only the results for Kinsmen Sport Centre building are included in this demo version. Then, users can select their parameter class of interest, including the fuel and topography or the fire behavior, as seen in Fig. 31a. Depending on the user's selections, further selections will be provided through another menu, which is shown in Fig. 31b. Note that fire behavior parameter class requires the user to select a specific date since they are updated results and date-dependent. Finally, the requested map will be generated upon the user's click on the bottom, which sample is presented in Fig. 31c. In addition, the GUI provides users with the option to download the generated maps.

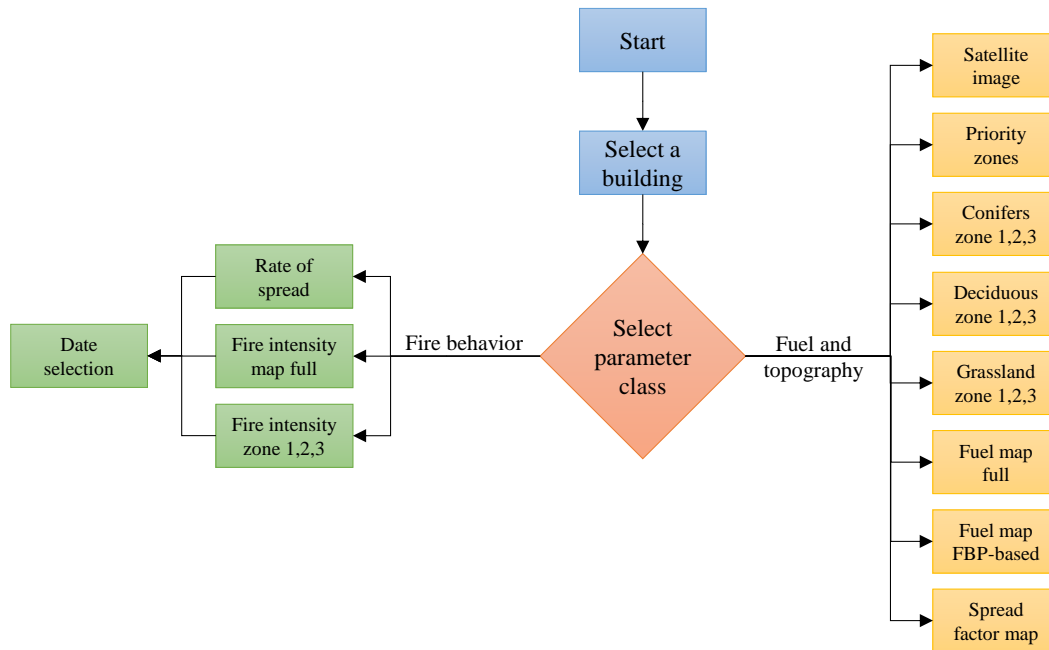


Fig. 29. User flow diagram for the proposed GUI

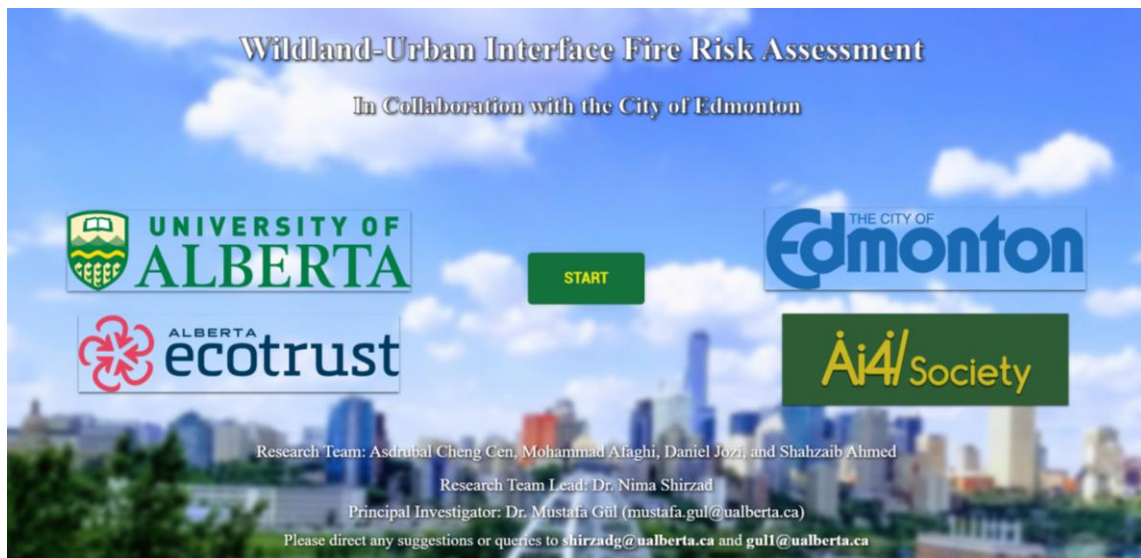


Fig. 30. GUI landing page, available at <https://uofa-combine-project.github.io/WUI-Fire-Risk-Assessment/>.



Fig. 31. Screenshots of the demo version of the GUI, accessible at <https://uofa-combine-project.github.io/WUI-Fire-Risk-Assessment/>.

6 Conclusions and Future Work

In this research, a combination of satellite imagery and street-level crowdsensing-based videos were employed to determine fire risks in Wildland-Urban Interface zones. This framework demonstrated that the automated segmentation and classification of vegetative fuels in satellite images is possible using convolutional neural networks (CNNs), and important fuel information such as heights or seasonal effects can be extracted using automated crowdsensing-based video analysis. Kinsmen Sport Centre building in Edmonton was selected as a location of interest in this study and all results were presented for the surrounding region.

In the satellite analysis stage, topographic analyses were conducted to determine priority zones around the building according to the National Guide for Wildland-Urban Interface Fires. In addition, CNNs were employed to automatically detect different fuel types of coniferous and deciduous trees as well as ground vegetation with high accuracy. Fuel classifications were then conducted according to the Fire Behavior Prediction (FBP) system.

In the crowdsensing analysis stage, street-level videos from car-mounted cameras were used to detect fuel characteristics that could not be seen through satellite imagery. These features are listed as the percent curing of the grass, the leafing condition of the deciduous, and the crown base height of the conifers. These parameters, combined with up-to-date weather information from weather stations, could be employed to create an updated fire intensity map for WUI zones following FBP procedures.

In the final stage, the data extracted from satellite and crowdsensing-based analyses were integrated into the FBP-based calculations to calculate parameters such as the Rate of Spread (ROS) and the Head Fire Intensity (HFI). These parameters provide insights toward the risk of WUI fires and provide valuable opportunities for decision-makers to mitigate fire hazards in urban areas.

The proposed framework has some limitations that could be investigated in future research studies. For instance, the model can be further developed by:

- Verifying and calibrating the results using empirical data from previously developed models.
- Improving the convolutional neural network to detect different types of conifers such as Jack spine and white/black spruce.
- Developing additional processes to extract weather data at a localized level such as relative humidity, temperature, wind speed, and others to have a micro-level map of the intermediate fire weather index parameters such as fine foliar moisture content, draught code, buildup index, etc.
- Developing the necessary algorithms to compute fire characteristics other than Rate of Spread (ROS) and Head Fire Intensity (HFI) such as:
 - Fire Description (Crown Fraction Burned and Fire Type)
 - Head, Flank, and Back Fire Spread Distances
 - Flank and Back Fire Rate of Spread
 - Flank and Back Fire Intensities
 - Elliptical Fire Area and Perimeter
 - Rate of Perimeter Growth
 - Length-to-Breadth Ratio
- Developing a system that can process different multiple crowdsensing sources to get more robust and reliable data and hence more comprehensive fire risk management.

7 Funding Acknowledgement

Funding support from Alberta Ecotrust and the City of Edmonton under the CitiesIPCC Grant Program (Grant # 2021-I-72-IPCC) is gratefully acknowledged. In addition, we are grateful to AI4Society at the University of Alberta for their partial financial support of this research.

References

1. Bénichou, N., Adelzadeh, M., Singh, J., Gomaa, I., Elsagan, N., Kinateder, M., Ma, C., Gaur, A., Bwalya, A., and Sultan, M. (2021). National Guide for Wildland-Urban Interface Fires. National Research Council Canada: Ottawa, ON. Available: <https://doi.org/10.4224/40002647>
2. Cohen, J. and Westhaver, A. (2022). An examination of the Lytton, British Columbia wildland-urban fire destruction. Institute for Catastrophic Loss Reduction: Toronto, ON. 56 pp. Available: <https://firesmartbc.ca/wp-content/uploads/2022/05/An-examination-of-the-Lytton-BC-wildland-urban-fire-destruction.pdf>
3. Kornik, S. (2016). Fire in Wolf Willow damages homes, one of several fires burning in Edmonton's River Valley Sunday. Global News. Available: <https://globalnews.ca/news/2688158/frightening-moments-for-west-edmonton-residents-as-brush-fire-nearly-advances-into-neighbourhood/>
4. Ohler, Q. (2023). Fire crews called to blaze in Edmonton's river valley. Global News. Available: <https://globalnews.ca/news/9657939/fire-crews-called-to-blaze-in-edmontons-river-valley/>
5. Anderson Hal, E. (1982). Aids to determining fuel models for estimating fire behaviour. USDA For. Serv. Gen. Tech. Rep. INT-122, 22p. *Intermt. For. and Range Exp. Stn.*. Ogden, Utah. 84401. Available: https://www.fs.usda.gov/rm/pubs_int/int_gtr122.pdf
6. Van Wagner, C.E. (1987). Development and structure of the Canadian Forest Fire Weather Index System. Canadian Forestry Service: Ottawa. *Forestry Technical Report*. Vol. 35. Available: <https://d1ied5g1xfgpx8.cloudfront.net/pdfs/19927.pdf>
7. Feng, Q., Liu, J., and Gong, J. (2015). UAV remote sensing for urban vegetation mapping using random forest and texture analysis. *Remote sensing*. vol. 7. no. 1. pp. 1074–1094.
8. Stubbings, P., Peskett, J., Rowe, F., and Arribas-Bel, D. (2019) A hierarchical urban forest index using street-level imagery and deep learning. *Remote Sensing*. vol. 11. no. 12, p. 1395.
9. Li, S., Dragicevic, S., Castro, F. A., Sester, M., Winter, S., Coltekin, A., Pettit, C., Jiang, B., Haworth, J., Stein, A., and Cheng, T. (2016) Geospatial big data handling theory and methods: A review and research challenges. *ISPRS journal of Photogrammetry and Remote Sensing*, vol. 115. pp. 119–133.
10. Berland, A., and Lange, D. A. (2017) Google street view shows promise for virtual street tree surveys. *Urban Forestry & Urban Greening*. vol. 21. pp. 11–15.

11. Ma, L., Liu, Y., Zhang, X., Ye, Y., Yin, G., and Johnson, B. A. (2019) Deep learning in remote sensing applications: A meta-analysis and review. *ISPRS journal of photogrammetry and remote sensing*. vol. 152. pp. 166–177.
12. Seiferling, I., Naik, N., Ratti, C., and Proulx, R. (2017) Green streets- quantifying and mapping urban trees with street-level imagery and computer vision. *Landscape and Urban Planning*. vol. 165. pp. 93–101.
13. Li, X., Ratti, C., and Seiferling, I. (2017) Mapping urban landscapes along streets using google street view. in *Advances in Cartography and GIScience: Selections from the International Cartographic Conference*. No. 28. pp. 341–356.
14. Laumer, D., Lang, N., Van Doorn, N., Mac Aodha, O., Perona, P., and Wegner, J. D. (2020) Geocoding of trees from street addresses and street-level images. *ISPRS Journal of Photogrammetry and Remote Sensing*. vol. 162. pp. 125–136.
15. Wegner, J. D., Branson, S., Hall, D., Schindler, K., and Perona, P. (2016) Cataloging public objects using aerial and street-level images-urban trees. in *Proceedings of the IEEE Conference on Computer Vision and Pattern Recognition*. pp. 6014–6023.
16. Natural Resources Canada. (2017) Topographic Data of Canada - CanVec Series. Open Government Portal. Available: <https://open.canada.ca/data/en/dataset/8ba2aa2a-7bb9-4448-b4d7f164409fe056>
17. Wright JG. (1938). Grass-fire hazard tables for eastern Canada. *Lands, Parks and Forests Branch*.
18. Forestry Canada Fire Danger Group. (1992). Development and structure of the Canadian Forest Fire Behavior Prediction System. *Forestry Canada, Headquarters, Fire Danger Group and Science and Sustainable Development Directorate, (Ottawa)*. Information Report ST-X-3. Available: <https://d1ied5g1xfp8x8.cloudfront.net/pdfs/10068.pdf>
19. Beaudoin, A., Bernier, P. Y., Guindon, L.; Villemaire, P., Guo, X.J., Stinson, G., Bergeron, T., Magnussen, S., Hall, R.J. (2014). Mapping attributes of Canada's forests at moderate resolution through k NN and MODIS imagery. *Canadian Journal of Forest Research*. vol. 44(5). pp. 521–532. Available: <https://cdnsiencepub.com/doi/10.1139/cjfr-2013-0401>
20. Alipour, M., La Puma, I., Picotte, J., Shamsaei, K., Rowell, E.; Watts, A., Kosovic, B., Ebrahimian, H., Taciroglu, E. (2023). A Multimodal Data Fusion and Deep Learning Framework for Large-Scale Wildfire Surface Fuel Mapping. *Fire*. vol. 6. No. 2. p. 36.
21. López-De-Castro, M., Prieto-Herráez, D., Isabel Asensio-Sevilla, M., Pagnini, G. (2022). A high-resolution fuel type mapping procedure based on satellite imagery and neural networks: Updating fuel maps for wildfire simulators. *Remote Sensing Applications: Society and Environment*. vol. 27. p. 100810.

22. Food and Agriculture Organization of the United Nations. (2020). Global Forest Resources Assessment, Terms and Definitions. *FAO Forestry Department*. Rome, Italy. vol. 32. Available: <https://www.fao.org/3/I8661EN/i8661en.pdf>
23. Phelps, N., Cameron, H., Forbes, A.M. et al. (2022). The Alberta Wildland Fuels Inventory Program (AWFIP): data description and reference tables. *Annals of Forest Science*. vol. 79. no. 28.
24. Azim Md. R., Keskin M., Do N., and Gül M. (2022) Automated classification of fuel types using roadside images via deep learning. *International Journal of Wildland Fire*. vol. 31. pp. 982-987.
25. Bewley, A., Ge, Z., Ott, L., Ramos, F. and Upcroft, B. (2016). Simple online and realtime tracking. *IEEE International Conference on Image Processing (ICIP)*. Phoenix, AZ, USA. pp. 3464-3468.
26. Beverly, J. L., Sonja E. R. Leverkus, Hilary Cameron, and Dave Schroeder. (2020). Stand-Level Fuel Reduction Treatments and Fire Behaviour in Canadian Boreal Conifer Forests. *Fire*. vol. 3. no. 3:35.
27. Visvalingam, M. and Whyatt, J.D. (1990) The douglas-peucker algorithm for line simplification: Re-evaluation through visualization. *Comput. Graph. Forum*. vol. 9. pp. 213–225.
28. Wright JG. (1938). Grass-fire hazard tables for eastern Canada. Lands, Parks and Forests Branch.
29. Fridman L, Terwilliger J, Jenik B. (2018). Deeptraffic: Crowdsourced hyperparameter tuning of deep reinforcement learning systems for multi-agent dense traffic navigation. arXiv preprint:1801.02805.
30. Garvey M and Millie S. (2000) Grassland Curing Guide. *Country Fire Authority, Community Safety Department, Melbourne, Australia*. Available: <https://www.cfa.vic.gov.au/ArticleDocuments/1481/grassland-curing-guide.pdf.aspx>
31. National Wildland Coordinating Group. (2021). CFFDRS System Overview. Available: <https://www.nwcg.gov/publications/pms437/cffdrs/overview>
32. Oregon State University. (2023). Mapping Wildfire Risk to Structures and other Human Developments. *College of Forestry*. Available: <https://osuwildfireriskmap.forestry.oregonstate.edu/mapping-wildfire-risk-structures-and-other-human-developments>